Energy Advances

Accepted Manuscript

This article can be cited before page numbers have been issued, to do this please use: A. Augustin, M. S. Yesupatham, M. D. Dhileepan, S. Son, E. Ravindran, N. Bernaurdshaw, H. Kim and K. Sekar, *Energy Adv.*, 2024, DOI: 10.1039/D4YA00476K.

ROYAL SOCIETY OF CHEMISTRY

rsc.li/energy-advances

View Article Online
DOI: 10.1039/D4YA00476K

Construction of organic inorganic hybrid composite derived from C_3N_5 incorporated with CeO_2 for the enhanced photocatalytic hydrogen evolution

Ashil Augustin[a], Manova Santhosh Yesupatham[a], M.D. Dhileepan[a], Sanguk Son[b], Ezhakudiyan Ravindran[a], Bernaurdshaw Neppolian[a], Hyoungil Kim[b*], and Karthikeyan Sekar[a*]

[a]*Department of Chemistry, Faculty of Engineering and Technology, SRM Institute of Science and Technology, Kattankulathur, 603203, India*

[b]*Department of Civil & Environmental Engineering, Yonsei University, Seoul 03722, Republic of Korea*

Corresponding Author E-mail: karthiks13@srmist.edu.in; hi.kim@yonsei.ac.kr

Abstract

The concern regarding energy scarcity and environmental issues are effectively addressed by the photocatalytic hydrogen production. The effective combination of semiconductor materials can prevent exciton recombination, making it a highly effective method to enhancing photocatalytic activity. This report details the synthesis of conjugated polymer, encapsulated with metal oxide photocatalyst using a simple ex-situ method. The encapsulation of polymer with CeO_2 nanoparticles results in exceptional performance in H_2 production, which exhibit improved visible light absorption and a significant increase in charge transfer efficiency. This is accredited to the high charge transfer and reduced recombination in the composite. Moreover, the photogenerated holes leads a substantial decline in the recombination rate of excitons, and concomitant enhancement in the rate of photocatalytic H_2 production. Important to note that, the observed hydrogen evolution, at around 10 wt.% of CeO_2 doped C_3N_5 composites is 1256 μmol/g/h, whereas C_3N_5 125 μmol/g/h alone. Electrochemical analysis showed that the optimized composites exhibit a low electron-hole recombination rate and the UV-Vis spectra analysis shows an improved visible light absorption, resulting an excellent photocatalytic activity. Notably, the proposed system is the first report on hydrogen evolution *via* photocatalysis using CeO_2/C_3N_5 composites. Consequently, this research offers a new perspective on the design of organo inorganic heterostructures and introduces a novel pathway to exploring their catalytic capabilities.

Introduction

View Article Online
DOI: 10.1039/D4TA00476K

Fossil fuels, including crude oil, natural gas, and coal are contributes an essential role to satisfy the world's energy needs.[1, 2] From 2024 to 2050, it is anticipated that global energy consumption will increase by nearly 55% and CO_2 emissions by 20%.[3, 4] The global warming and fuel shortages that have resulted from the significant increase in the emission of greenhouse gases and the accelerated depletion of fossil fuels have compelled humanity to identify alternative renewable and pure energy sources.[5] It is anticipated that the consumption of renewable energy will increase and reach approximately 247 exajoules by 2050. In contrast, the total consumption of renewable energy was 96 exajoules in 2024.[6] Photocatalytic water splitting using semiconductors has been recognized as a sustainable and prospective green technology that has garnered significant attention due to its ability to effectively convert sustainable solar energy into environmentally friendly hydrogen. A sustainable method of producing green hydrogen fuel is through photocatalytic water splitting, which utilizes pure solar energy.[7-9] Due to it is environmentally friendly and sustainable nature, photocatalysis has garnered significant interest among many other potential technologies. It is designed for the way that plants use their photosynthesis processes to transform low-density solar energy towards high-density energy fuels. [10-12] To achieve this, our research communities are working extremely hard to investigate the effective, reliable, affordable, and visible-light sensitive materials. Innovation based on photocatalysis is useful as a viable, sustainable energy, cost-effective, and reliable with a steady solution to the world's power issue.[13-15] Solar energy can be converted into sustainable hydrogen as an energy using photocatalytic water splitting using semiconductors irradiated by visible light, which is a safe and environmentally responsible process. Goodeve & Kitchener (1938) discovered the TiO_2 which can produce dye removal efficiency including both in vacuum & air conditions, while TiO_2 remained stable after a reaction completed, this marked the beginning of semiconductor-based photocatalysts.[16, 17] Fujishima and Honda (1972) noticed a photoelectrical water splitting on TiO_2 film when solar light was being irradiated and the door to semiconductor-based photocatalysts innovation was opened as soon as the world became aware of this amazing accomplishment.[18] However, the activity of the majority of photocatalysts was still constrained by the absence of active sites, severe recombination of photogenerated excitons, and diminished light-harvesting efficiency.[19, 20] Therefore, it was imperative to investigate novel photocatalysts with a broad spectral response that were extremely active to achieve sustainable hydrogen production. The modifiable band diagram, low-toxicity, good thermal stability, and chemical stability of graphite carbon nitride (g-C_3N_5) have all been the subject of extensive research. In addition to that, the visible light absorption can be expanded and a rapid electron movement can be

View Article Online
DOI: 10.1039/D4TA00476K

facilitated by the narrow band gap of g-C_3N_5.[21-26] CeO_2 is a type of rare earth metal oxide that is non-toxic, and low-cost having a cubic crystalline n-type material with 2.5 eV of band gap. In the CeO_2 unit cell, every Ce(IV) is linked in the octahedral interstitial with eight adjacent O^{2-}, and each O^{2-} is linked with four adjacent Ce(IV) forming a tetrahedral structure, here Ce^{3+} and Ce^{4+} are capable of coexisting indefinitely and converting to each other effortlessly.[27-29] The efficacy of photocatalysts will be improved resulting the multivalence property of CeO_2 which enable the generation of robust interactions with other catalyst components for photocatalytic hydrogen production. Zou et al., has developed CeO_2 hybridised g-C_3N_4 composite which produced a hydrogen yield of 860 μmol/g/h.[30] Sha et al., has discussed about the charge separation in CeO_2/MnO_2 nanoflakes with an efficiency of 540 μmol/g/h of hydrogen.[31] Liu et al. has modified C_3N_5 with nickel oxide for improving the activity which shows an yield of 357 μmol/g/h of hydrogen production.[32] Still, there are no pertinent reports regarding the formation of a heterojunction between C_3N_5 and CeO_2 for photocatalytic hydrogen evolution. The heterostructure obtained by the chemical binding of C_3N_5 and CeO_2 composites, which is effectively segregate and constrain the charge carrier recombination. As anticipated, the well-designed CeO_2/C_3N_5 heterojunction, substantially improve the photocatalytic hydrogen evolution, without the need of additional co-catalysts.

Materials

All chemicals and reagents 3-amino-1,2,4-triazole ($C_2H_4N_4$) (≥98%), Cerium (III) nitrate hexahydrate ($Ce(NO_3)_3.6H_2O$) (≥98%), Methanol (CH_3OH) (≥98%), Ethanol (CH_3CH_2OH) (≥99.5%), Triethanolamine ($C_6H_{15}NO_3$) (≥98%), Lactic Acid ($C_3H_6O_3$) (≥98%), Ascorbic Acid ($C_6H_8O_6$) (≥99%), Sodium Sulfide (Na_2S) (≥98%), Sodium Sulfite (Na_2SO_3) (≥98%) were obtained from Sigma Aldrich, TCI, and SRL India.

Synthesis of C_3N_5

C_3N_5 was synthesized by thermal polymerization method in a muffle furnace which was described in the literature by Wu et al. In the typical synthesis, 2 g of 3-amino-1,2,4-triazole was placed in a porcelain crucible and was gradually calcined at 550 °C with a heating rate of 2°C/min for a period of 3 hrs. Bulk C_3N_5 is in dark-yellowish product that was collected and crushed into a powder after naturally cooling to room temperature[33] (Scheme.1 a).

View Article Online
DOI: 10.1039/D4YA00476K

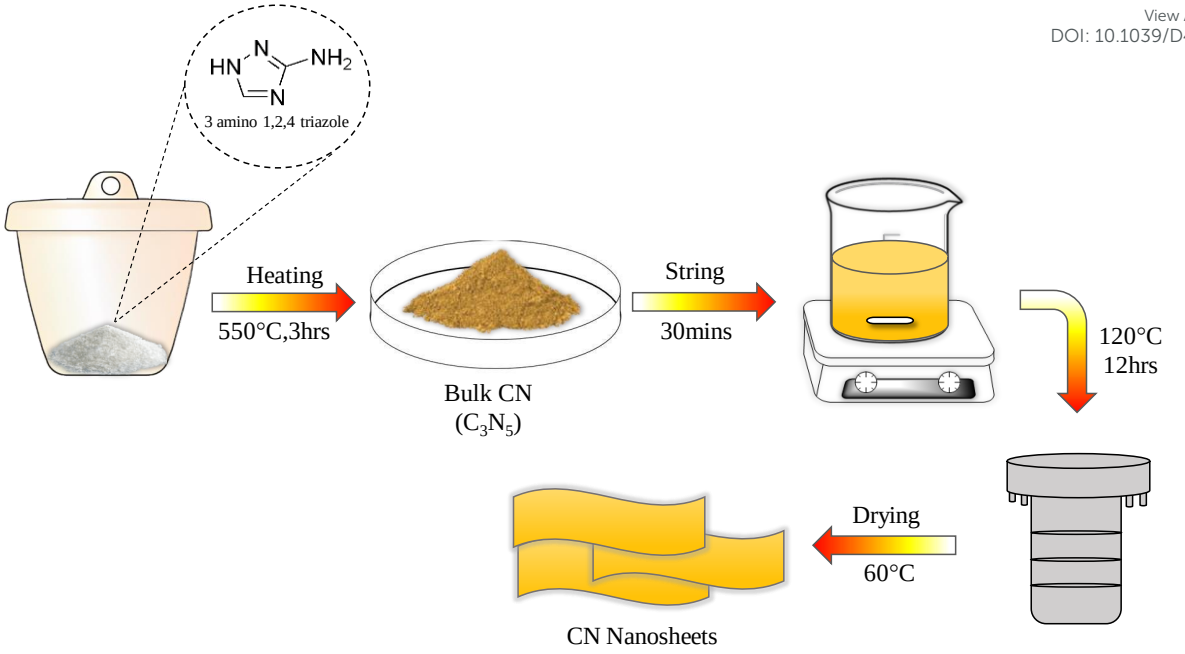

Scheme 1a). Schematic representation for the synthesis of C_3N_5

Synthesis of CeO_2

CeO_2 was synthesized by thermal polymerization method in a muffle furnace which was described in the literature Song et al. Briefly, 2.0g Cerium (III) nitrate hexahydrate ($Ce(NO_3)_3.6H_2O$) was calcined at 500 °C for 2 hrs in the muffle furnace with a heating rate of 2 °C/min. CeO_2 is in light-yellowish product that was collected and crushed into a powdered after naturally cooling to room temperature[34] (Scheme1b).

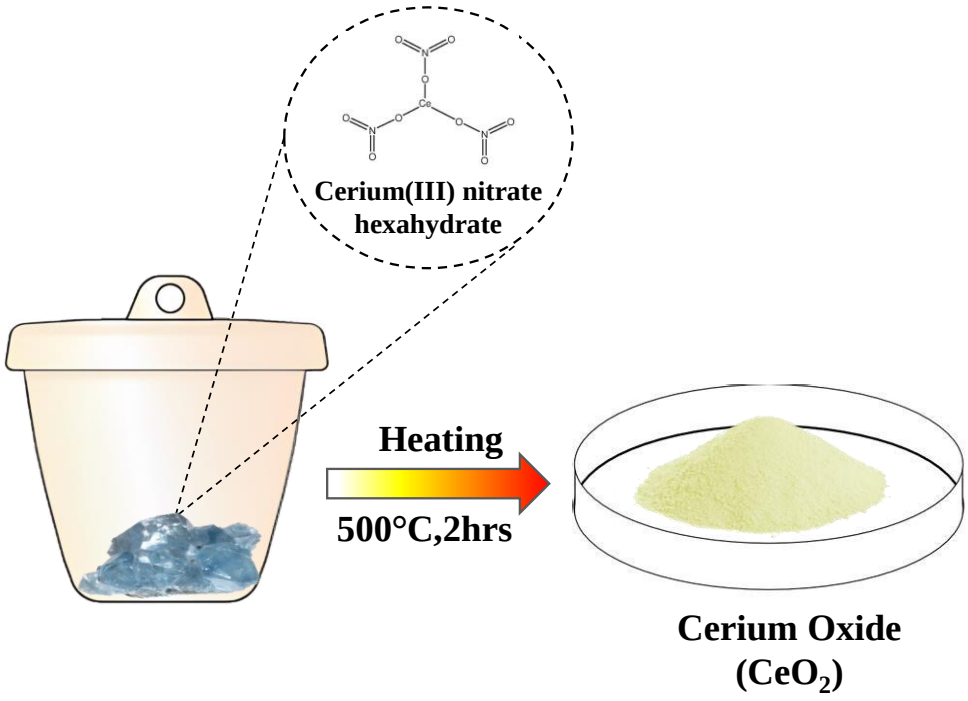

Scheme 1b) Schematic representation for the synthesis of CeO_2.

View Article Online
DOI: 10.1039/D4YA00476K

Synthesis of C_3N_5/CeO_2 Composite

The C_3N_5/CeO_2 heterostructures were synthesized as follows: 100 mg of C_3N_5 was mixed in 25 mL of methanol under an ultrasonic setting for 30 min, and then a sufficient amount of CeO_2 was immersed into the suspensions. The mixture was vigorously stirred at room temperature followed by half an hour of ultrasonic treatment to get rid of the organic solvent. The resultant dark yellowish powder was then calcined for 4 hrs at 100 °C with a 2°C/min heating rate. The composite catalysts were designated as 5wt.% C_3N_5/CeO_2, 10wt.% C_3N_5/CeO_2, 15wt.% C_3N_5/CeO_2, and 20wt.% C_3N_5/CeO_2 by various weight percentage of polymer content (5, 10, 15, 20 wt.%) in the composite (Scheme 1c). The term "C_3N_5/CeO_2" expressly refers to 10wt.% C_3N_5/CeO_2 in the subsequent text.

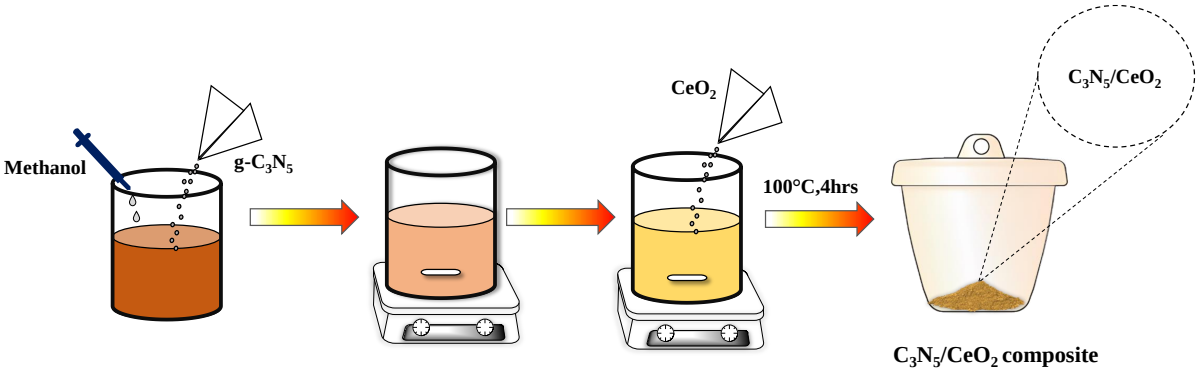

Scheme 1c) Schematic representation for the synthesis of C_3N_5/CeO_2 Composite.

Characterisation

The phase purity and crystallinity of the photocatalyst that was prepared were assessed through X-ray diffraction utilizing a PANalytical X'Pert particle diffractometer with Cu Kα radiation (λ = 1.5406 A). Shimadzu IRTracer-100 was used to carry out the Fourier-transform infrared spectrometer (FT-IR). The morphology of the nanocomposites was examined utilizing high-resolution transmission electron microscopy (HRTEM, JEOL Japan, JEM-2100 Plus) and Field Emission Scanning Electron Microscopy (FE-SEM) (FEI Quanta FEG 200). UV–vis diffuse reflectance (UV-DRS) data were acquired through the utilization of a Shimadzu UV-3600i Plus UV–vis spectrophotometer. Utilizing a fluorescence spectrophotometer (Horiba, Fluorolog-QM), the photoluminescence (PL) spectra were analysed.

View Article Online
DOI: 10.1039/D4YA00476K

Photoelectrochemical Measurements.

The CHI 760E electrochemical workstation was employed to acquire the Mott-Schottky, impedance and transient photocurrent response. Ag/AgCl and a Platinum wire serve as the reference and counter electrode respectively. As an electrolyte, a 0.5 M Na_2SO_4 aqueous solution is utilized. The slurry was prepared through the deposition of a 2.5 g of catalyst dispersed in a mixture of deionized water and anhydrous ethanol (1:1) and coated on the working electrode (glassy carbon electrode) for electrochemical studies.

Photocatalytic Studies

The photocatalytic hydrogen generation reaction was performed in direct sunlight. The reaction was carried out in a Kjeldhal flask containing 5 mg of the catalyst dispersed in 50 ml of 5% sacrificial agent. The dissolved gases were eliminated from the reaction solution by purging with nitrogen gas for 15 minutes. The reaction setup was kept under sunlight, and an offline gas chromatograph (Shimadzu GC-2014 equipped with a Molecular Sieve [5 A˚ column]) analysed hydrogen generation with a TCD detector after the reaction setup was kept in sunlight for a period of 3 hours. The mean solar light intensity was ascertained to be 80,000 lux using a lux meter. While the pH of the reaction mixture was adjusted using solutions of NaOH and H_2SO_4, various sacrificial agents were employed when necessary.

View Article Online
DOI: 10.1039/D4YA00476K

Results and discussion

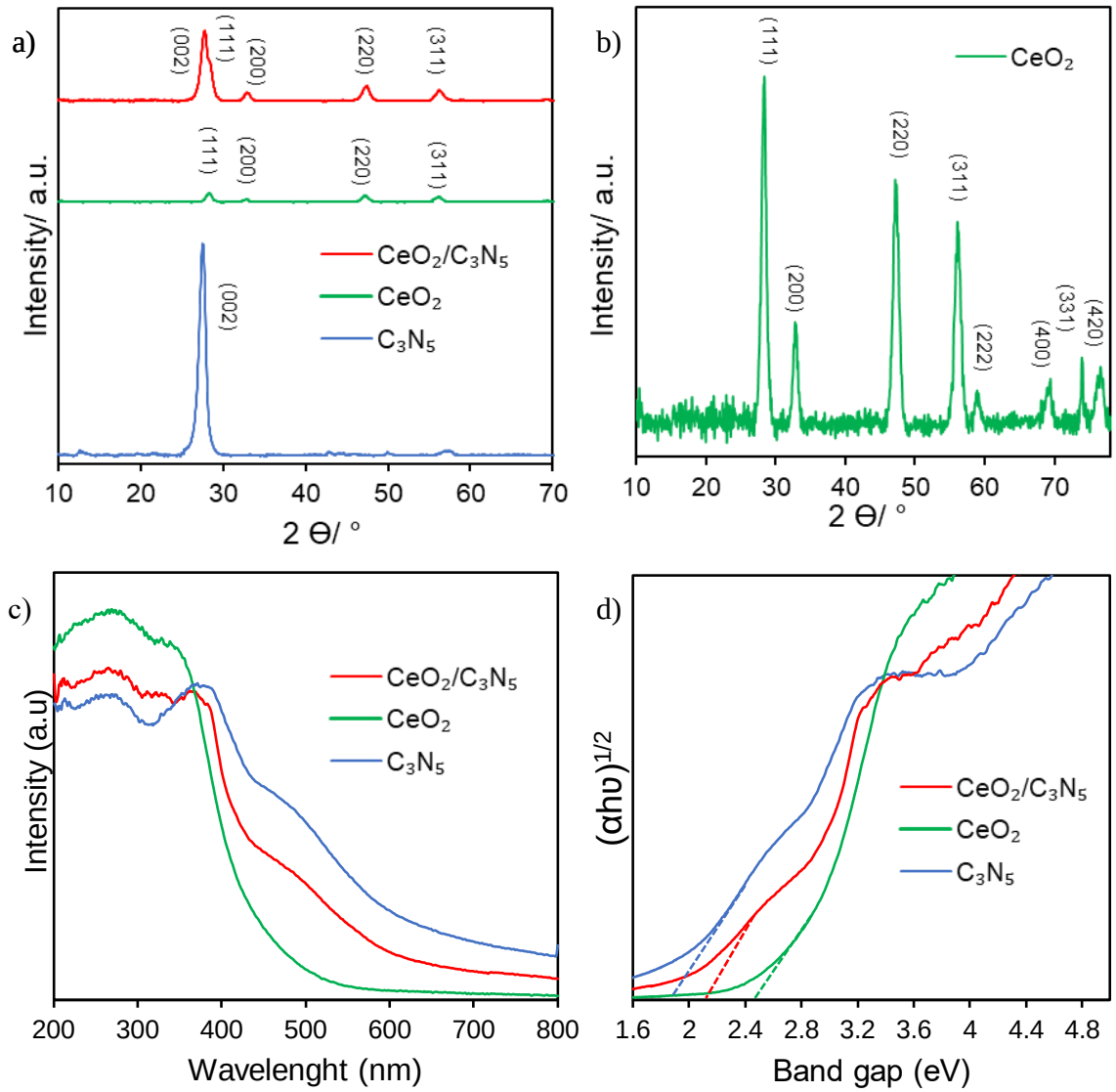

Figure 1. (a) XRD patterns of the C_3N_5, CeO_2 and CeO_2/C_3N_5composite, (b) XRD patterns of the CeO_2, (c) UV−vis absorbance spectra (d) optical band gap using relative Tauc plots.

Figure 1, shows the crystal structures of CeO_2, C_3N_5, and the 10wt% CeO_2/C_3N_5 nanocomposite are revealed by the XRD patterns (Figure 1a). Peaks in the CeO_2 XRD pattern can be found at 28.6°, 33.1°, 47.5°, 56.4°, and 59.1°, 69.2°,76.6° and 79.2° which correspond to the fluorite crystal structure's (111), (200), (220), (311), (222), (400), (331) and (420) planes, respectively (JCPDS 34-0394). (Figure 1b). The large peak (002) in the C_3N_5 XRD pattern, which is centered at 27.5 degrees, reveals the material's amorphous nature (JCPDS 87-1526). The CeO_2/C_3N_5 nanocomposites XRD pattern reveals peaks that correlate to the synthesis of

View Article Online
DOI: 10.1039/D4TA00476K

both CeO_2 and C_3N_5. Rietveld analysis of CeO_2 is obtained for understanding the atomic percentage of the elements (Figure S1). Composition. In the nanocomposite, the peak intensities of CeO_2 increased it is observed that C3N5's peak intensity is decreased, indicating some degree of crystallographic disorder brought on by the addition of C_3N_5. The stretching vibration of the surface free amino group and the hydroxyl group of water is represented by the wide peak of pure C_3N_5 at 3000–3600 cm^{-1} in (Figure S2). The typical stretching vibration of C-N and C-N heterocycles is responsible for the peaks at 1235 cm^{-1}, 1316 cm^{-1}, 1411 cm^{-1}, 1571 cm^{-1}, and 1637 cm^{-1}. The characteristic stretching vibration of the s-triazine ring unit is represented by the peak at 805 cm^{-1}. The characteristic peaks of C_3N_5 and CeO_2 remained unaltered in the composite, as evidenced by the presence of all characteristic vibration peaks in the corresponding CeO_2/C_3N_5 composites.

The UV-Vis diffuse reflectance spectra of the modified samples are illustrated in Figure 1(c). The CeO_2 shows an absorption below 500 nm is observed. Nevertheless, the photo response of exposed CeO_2 is expanded to the visible region when it is combined with C_3N_5. The band gap positions of CeO_2 and g-C_3N_5 are calculated as 2.5 eV and 1.9 eV, respectively, using the tauc plot, as illustrated in Figure 1(d). This may be attributed to the fact that C_3N_5 effectively functions in absorbing significant quantities of visible light particles. This confirms the efficacy of C_3N_5 for the purpose of visible light harvesting.

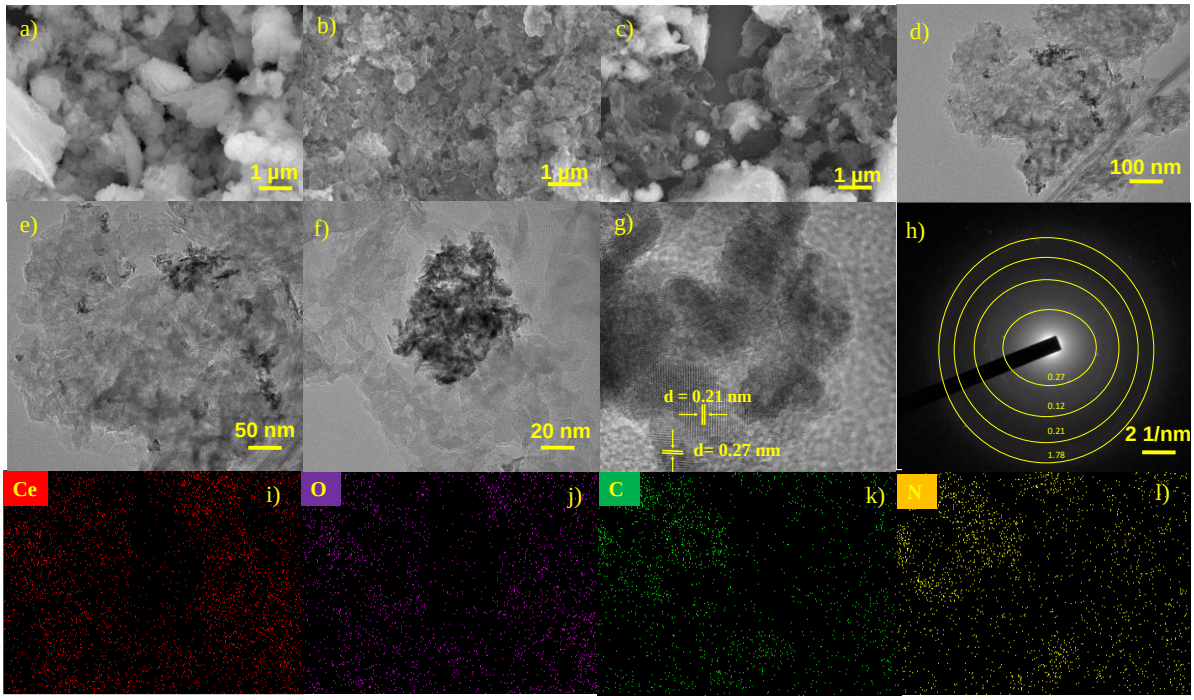

View Article Online
DOI: 10.1039/D4YA00476K

Figure 2. SEM images of (a) CeO_2, (b) C_3N_5 (c) CeO_2/C_3N_5 composite (d), (e), (f) and (g) high-resolution TEM (HRTEM) image of CeO_2/C_3N_5 composites, (g) and (h) clear fringes with lattice spacings. (i-l) EDS mapping images of Ce, O, C, and N elements.

The morphologies of CeO_2, C_3N_5 and CeO_2/C_3N_5 have been closely observed using SEM analysis. The SEM images show the presence of both CeO_2 incorporated onto C_3N_5. The impact of the CeO_2 on the morphological structure of C_3N_5 is clearly visible in the composite (Figure 2(a-c)). The TEM images reveal the composite formation between CeO_2 and C_3N_5 in Figure 2(e-g). As demonstrated, the micromorphology of g-C_3N_5 sheets is clearly observed and the presence of CeO_2 particles are obtained. The influence of CeO_2 decorated on the structure of C_3N_5 is clearly visible in the TEM images. The Figure. 2(e) shows clear (111) and (220) crystal planes with the lattice fringes with a spacing of 0.21 nm and 0.27 nm, respectively. The crystallite size of CeO_2 and C_3N_5 is calculated as 7.13 nm and 8.55 nm is obtained (Table S2). The acquired images confirmed the existence of crystallized CeO_2 nanoparticles encircled by an exceedingly thin layer of C_3N_5, which reflects the composite's extremely low concentration. (Figure S3). The images show that the CeO_2 nanoparticles were evenly distributed on the host photocatalyst, which shows that the CeO_2 nanoparticles were evenly distributed on the host photocatalyst, which is a sign of a good deposition process.

View Article Online
DOI: 10.1039/D4YA00476K

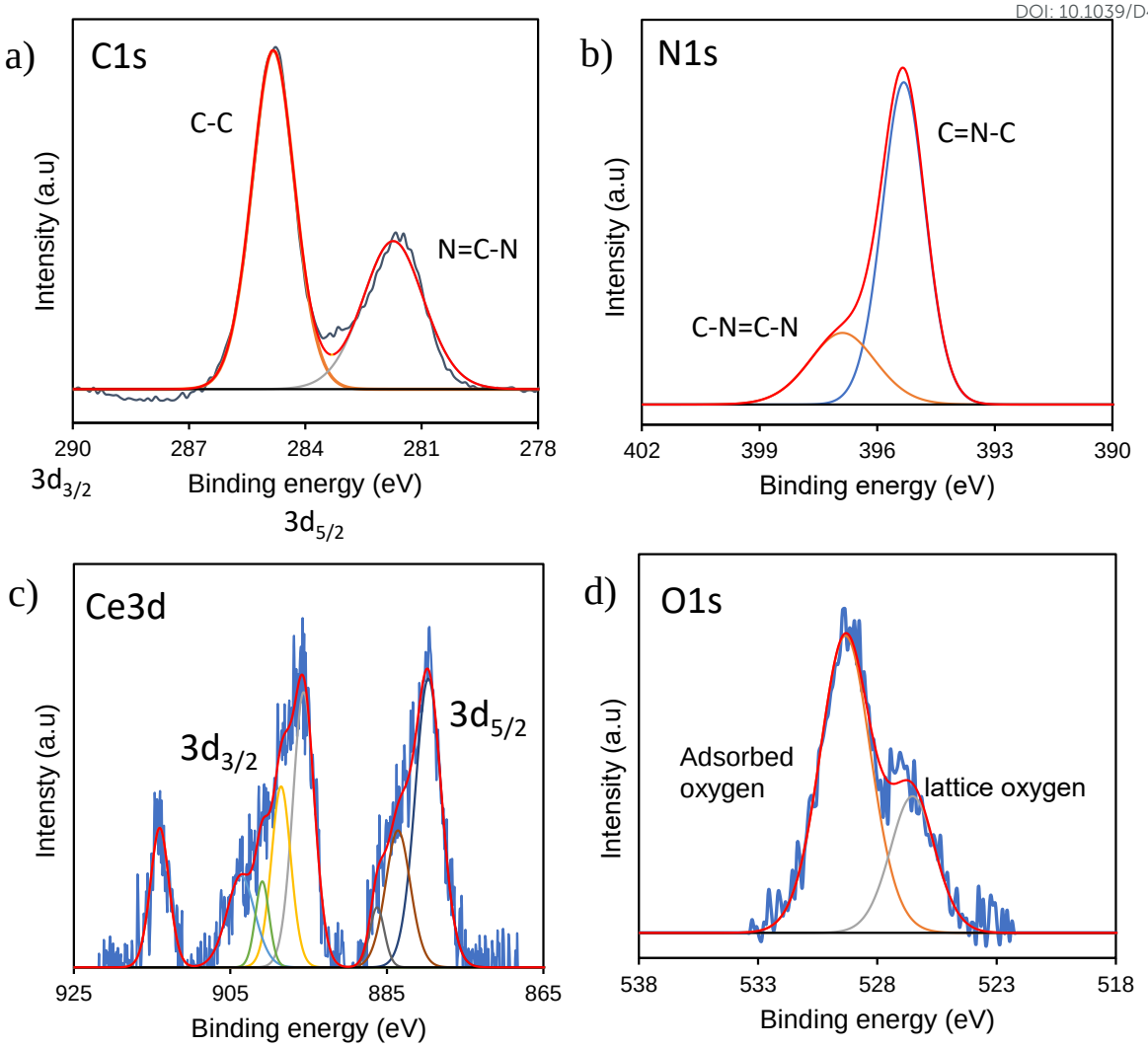

Figure 3. high resolution XPS of (a) C1s, (b) N 1s, (c) Ce 3d, (d) O 1s spectra of CeO_2/C_3N_5 composites.

By employing X-ray photoelectron spectroscopy (XPS), the electronic chemical states and surface element composition of CeO_2, C_3N_5 and CeO_2/C_3N_5 were ascertained (Figure 3). The CeO_2, C_3N_5 and CeO_2/C_3N_5 composite, as indicated by the XPS survey spectra presented in Figure S4, comprises the elements Ce, O, C and N. In the C1s spectra of C_3N_5 depicts that the binding energies at 284.9 eV, 287.6 eV and 288.3 eV correspond to C-C/C=C, N=C and C-NH bonds, respectively. In the high resolution of N 1s spectra, two main peaks at 402.3 eV and 404.1 eV are attributed to CN=C and C-N=N-C groups, respectively. In addition, the peak at 406.9 eV is generated by N-H bonds. The O1s spectra the peak labelled at 528.8 eV is attributed to the lattice oxygen in CeO_2. Apart from this a broad peak is deconvoluted at 532.3 eV and 538 eV which is attributed to oxide defects and adsorbed oxygen respectively. According to the high resolution of Ce 3d spectra of CeO_2 have been deconvoluted. Ce^{4+} is the dominating

View Article Online
DOI: 10.1039/D4YA00476K

state, and its characteristic spectrum is represented by the peak with high intensity at 914.2 eV. Furthermore, the Ce $3d_{5/2}$ spin orbit is represented by the peaks at 879.8 eV, 884.7 eV and 887.1 eV. The Ce $3d_{3/2}$ spin orbit is shown by the peaks at 903.7 eV, 900.4 eV, 899.3 eV, and 895.4 eV measurements (Figure S5). The sample surface was not completely oxidized, as evidenced by the presence of Ce^{3+}/Ce^{4+} oxidation states on the surface of CeO_2/C_3N_5 composites (Table S2).

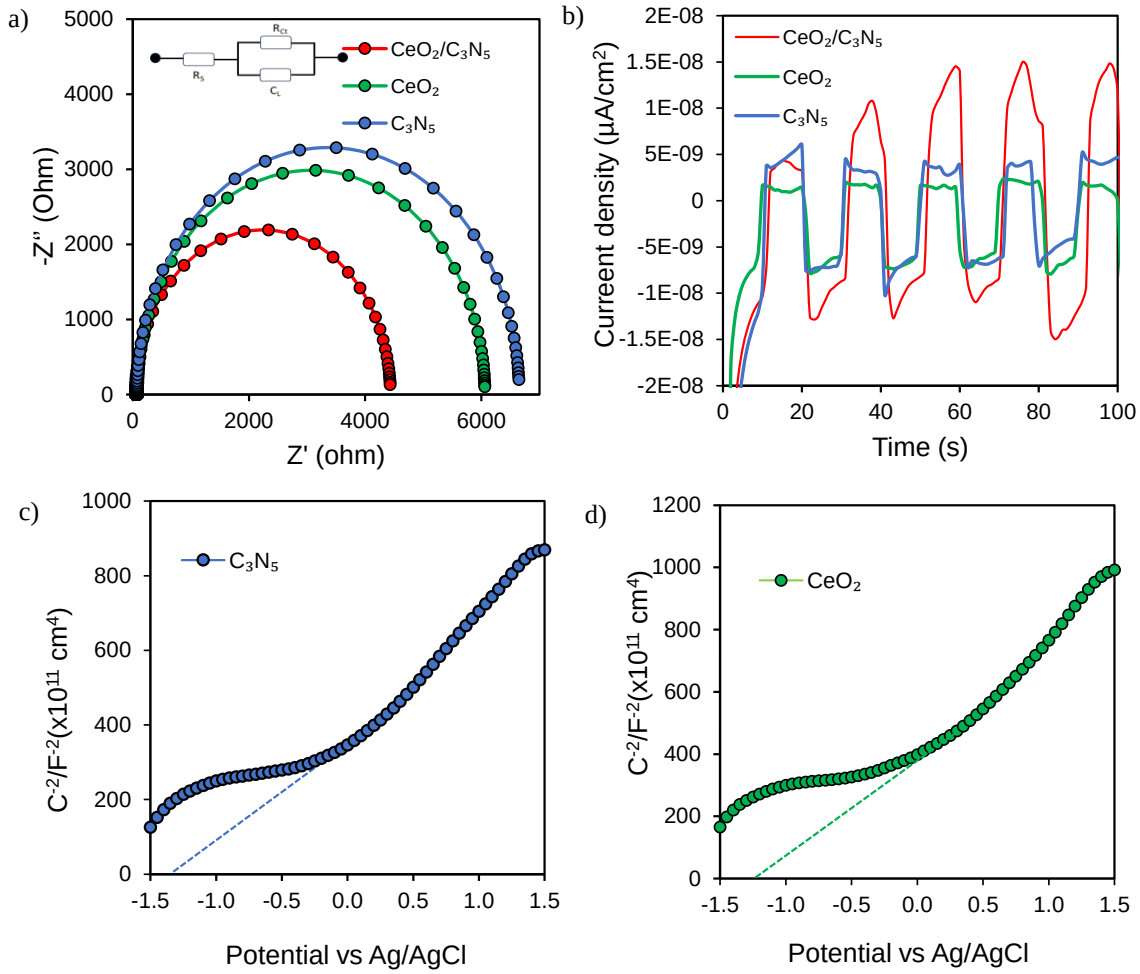

Figure 4 (a) Impedance spectra plots, (b) photocurrent response, (c) and (d) Mott−Schottky analysis of the samples.

The composite CeO_2/C_3N_5 is more mobile and has a greater resistance to charge recombination, as indicated by the reduced arc radius of the electrochemical impedance spectroscopy (EIS) Nyquist plot in comparison to that of CeO_2 and C_3N_5 (Figure 4a). Mott-Schottky analyses were performed on CeO_2 and g-C_3N_5 to clarify the flat band potential of the pristine materials. The

View Article Online
DOI: 10.1039/D4TA00476K

possibility existed that the positive slope represented an n-type semiconductor (Figure 4c) and 4 d)). In contrast to the redox potential of H^+/H_2, the flat band positions of C_3N_5 and CeO_2 concerning the Ag/AgCl electrode were -1.42 eV and -1.08 eV, respectively, both of which were more negative (Equation S1). The conduction band potential (CB) and flat band in n-type semiconductors are well established. Additionally, as demonstrated by the transient photocurrents in Figure 4(b), CeO_2/C_3N_5 demonstrates a significantly higher photocurrent density than the pristine materials when subjected to intermittent light irradiation. The CeO_2/C_3N_5 nanocomposite's improved charge transfer and separation efficacy is illustrated by its increased photocurrent response, which is accompanied by a decreased rate of photogenerated charge carrier recombination. The composite's PL intensity is lower than that of individual counterparts, which implies that it has a higher charge carrier separation efficiency (Figure S6). In summary, the photoelectrochemical data indicated that the photoelectron transport efficacy of the catalyst can be enhanced through the formation of a CeO_2/C_3N_5 nanocomposite.

Photocatalytic activity

In the presence of a hole scavenger in deionized water, the photocatalytic efficiency was evaluated in response to direct sunlight (Figure 5).

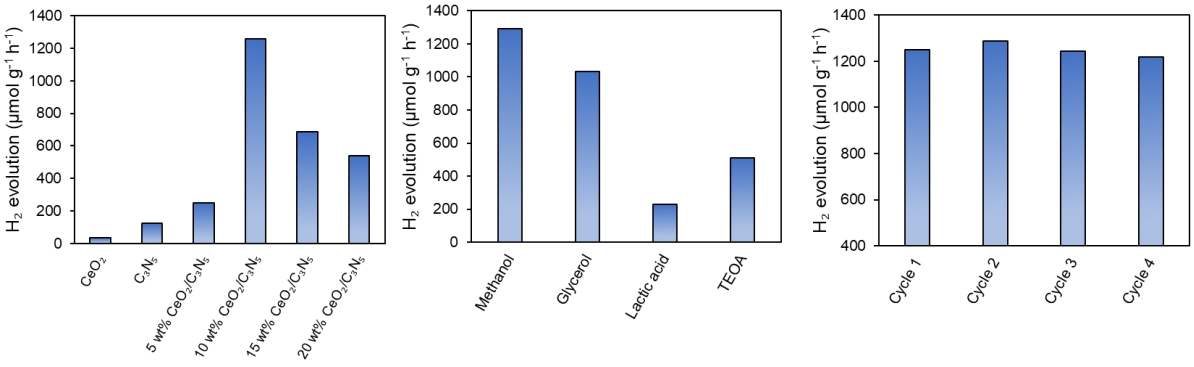

Figure 5. (a) Photocatalytic H_2 evolution rates of CeO_2/C_3N_5 composite, (b) Photocatalytic H_2 evolution rate with different scavengers, (c) Stability study.

The optimised CeO_2-C_3N_5 composite exhibits notable photocatalytic activity has been carried by using pristine CeO_2, C_3N_5, 5 wt.% CeO_2/ C_3N_5, 10 wt.% CeO_2/ C_3N_5, 15 wt.% CeO_2/C_3N_5, and 20 wt.% CeO_2/C_3N_5 composites. The 10 wt.% CeO_2/C_3N_5 composite has produced an

efficiency of 1256 μmol/g/h (Figure 5a). This value is considerably greater than that of the pristine material (125 μmol/g/h) and other composites. With increasing CeO_2, the rate of H_2 evolution initially increases and then decreases. Under visible-light irradiation, the H_2 evolution rate of the 10wt% CeO_2/C_3N_5 heterojunction can reach its maximal value when the loading amount of CeO_2. The results obtained is comparatively higher than that of the published articles in the field of photocatalytic hydrogen production which is discussed in table S1. The photocatalytic hydrogen evolution has carried out using different scavengers including methanol, TEOA, glycerol and lactic acid which produces a yield of 1290, 510, 1032, and 227 μmol/g/h (Figure 5b). In order to demonstrate the stability of catalyst, the CeO_2/C_3N_5 sample was subjected to four consecutive cycles (Figure 5c), the outcomes shows that the sample exhibits high stability and hydrogen production. XRD characterization studies confirms the structural integrity of the catalyst after repeated use (Figure S8).

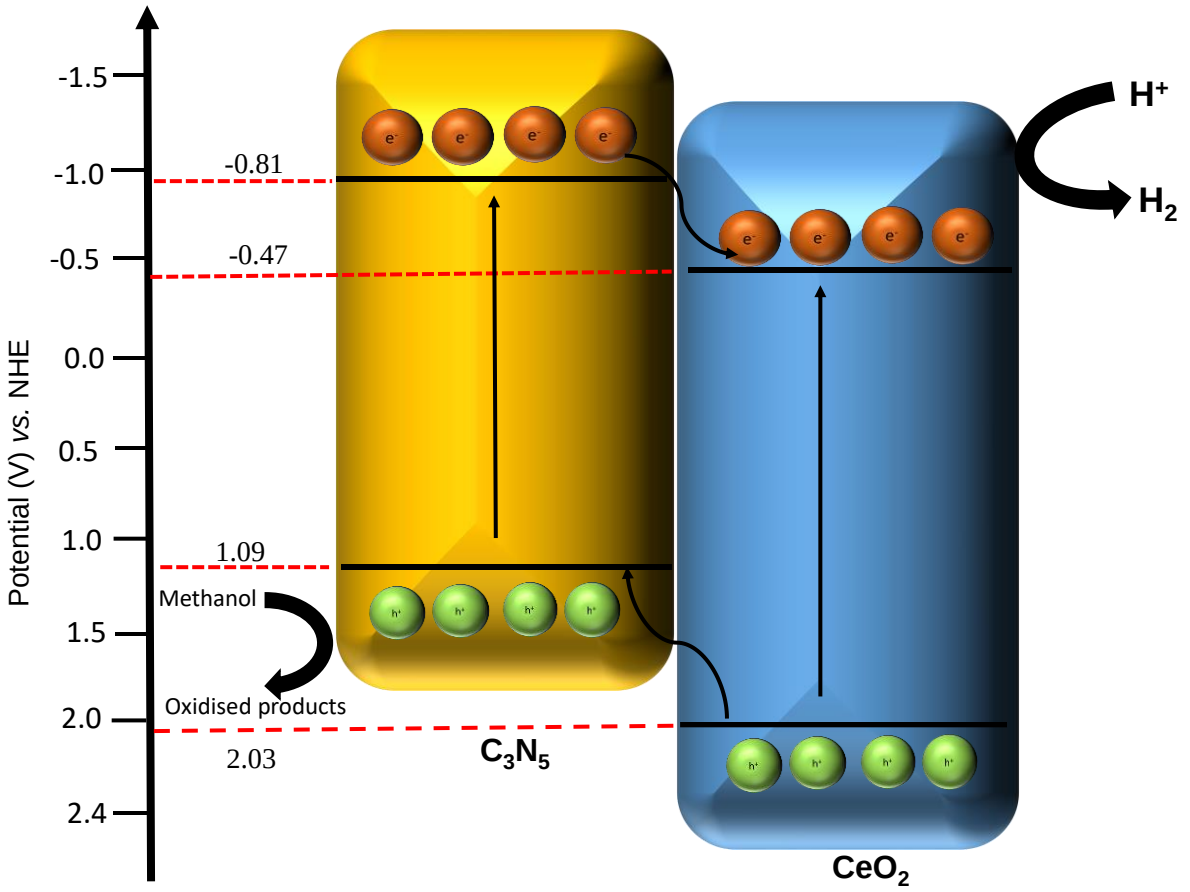

Figure 6. Plausible mechanism of the CeO_2/C_3N_5 catalyst.

Finally, on the basis of understanding the electronic charge transfer and the advantages of C_3N_5 for integrating with CeO_2 and forming type II heterojunctions were understood in light of the aforementioned results and prior experimental investigations. A potential mechanism for 10 wt.% CeO_2/C_3N_5 composites was suggested in (Figure 6) based on the observed results. e- is excited from the valence band (VB) to the conduction band (CB) of C_3N_5 and CeO_2 by high-energy photons under light irradiation. Using the Mott Schottky analysis the flat band positions of C_3N_5 and CeO_2 with respect to the Ag/AgCl electrode were -1.42 eV and -1.08 eV, respectively, in contrast to the redox potential of H^+/H_2. The relationship between the flat band and the conduction band potential (CB) in n-type semiconductors is well-established. The conduction band edges were -0.81 eV and -0.47 eV which is calculated from tauc plot analysis. (Equation S2). Therefore, a type II heterojunction mechanism was suggested for the CeO_2/C_3N_5 in response to the band levels of C_3N_5 and CeO_2. The conduction band accumulates excited electrons (e^-) in response to photon irradiation, while the valence band of C_3N_5 and CeO_2 accumulates holes (h^+). Due to variations in energy levels, the electrons that have accumulated migrate from the CB of C_3N_5 to the CB of CeO_2. At the same time, the openings from the valence band of CeO_2 are transferred to the valence band of C_3N_5. At the CB of CeO_2, the reduction of H^+ to hydrogen occurs concurrently, while the oxidation of hole scavenger occurs at the VB of C_3N_5. Consequently, the synergistic effect of C_3N_5 and CeO_2 can effectively separate photoelectron-hole pairs, thereby enticing a greater number of carriers to participate in the photodegradation process thereby improving the photocatalytic activity.

Conclusion

In summary, the CeO_2 dopedC_3N_5 composite is the product of a straightforward synthesis method, which led to the successful development of CeO_2-incorporated C_3N_5. The primary goal of this research is to investigate the impact of the organo inorganic hybrid photocatalysts by optimizing the catalyst to enhance the reaction mechanism. According to the results of the morphological investigation, the composition and morphological transformation of the synthesized samples are significantly affected by the CeO_2 dispersed on C_3N_5. Moreover, the optical band gap decreased, leading to an increased absorption of the visible spectrum. In addition, photoelectrochemical methods have consistently exhibited an effective ability to prevent the recombination of photogenerated electron-hole pairs. Notably, the photocatalytic hydrogen evolution for approximately 10 wt.% CeO_2 doped C_3N_5 catalyst is 1256 μmol/g/h, which is 10 times greater than that of C_3N_5 alone (125 μmol/g/h). Due to the efficient transfer

View Article Online
DOI: 10.1039/D4TA00476K

of photogenerated holes, the recombination rate of excitons has been significantly reduced and simultaneous enhancement of the rate of photocatalytic H_2 production occurred. This study offers a unique perspective that aids in the creation of innovative photocatalysts for efficient solar energy conversion into fuel.

Supporting information

Figure S1. Rietveld analysis of CeO_2 photocatalyst and composition of the CeO_2 photocatalyst, **Figure S2**. FTIR spectra of C_3N_5, CeO_2 and C_3N_5/CeO_2 Composite, **Figure S3.** a) SEM image (b-c) respective energy-dispersive spectroscopy ratio of the CeO_2/C_3N_5 composite (Ce, O, C, and N elements), **Figure S4.** Survey XPS spectra of CeO_2, C_3N_5 and C_3N_5/CeO_2 composite, **Figure S5.** high resolution XPS of (a) C1s, (b) N 1s, (c) Ce 3d, (d) O 1s spectra of CeO_2 and C_3N_5 pristine materials, **Figure S6.** photoluminescence spectra of the samples **FigureS7.** Mott−Schottky analysis of the samples a) CeO_2 b) C_3N_5, **Figure S8.** XRD analysis of C_3N_5/CeO_2 composite after and before the reaction study, **Table S1.** Physiochemical properties of the pristine catalyst used for photocatalytic application, **Table S2.** Elemental composition of C_3N_5, CeO_2 and C_3N_5/CeO_2 Composites, **Table S3.** Activity comparison of some representative photocatalysts for photocatalytic hydrogen production.

Acknowledgments

The authors appreciate the support from SRM Institute of Science and Technology, India. S.K. would like to thank the Royal Society-Newton International Fellowship Alumni follow-on funding support AL\211016 and AL\221024. S.K. also thanks to the SERB Start-up Research Grant (SRG/2023/000658). We acknowledge SRMIST for providing fellowship, SRM-SCIF, and Nanotechnology Research Centre (NRC) for providing the research facilities

Conflicts of Interest

The authors declare no conflict of interest.

References

1. S. Chu and A. J. n. Majumdar, *nature*, 2012, **488**, 294-303.
2. T. Hisatomi and K. J. N. C. Domen, *Nature Catalysis*, 2019, **2**, 387-399.
3. L. Wang, S. Duan, P. Jin, H. She, J. Huang, Z. Lei, T. Zhang and Q. J. A. C. B. E. Wang, *Applied Catalysis B: Environmental*, 2018, **239**, 599-608.

View Article Online
DOI: 10.1039/D4TA00476K

4. A. Naldoni, M. Altomare, G. Zoppellaro, N. Liu, S. Kment, R. Zboril and P. J. A. c. Schmuki, *ACS catalysis*, 2018, **9**, 345-364.
5. X. Yin, X. Zhao and W. J. E. Zhang, *Energy*, 2018, **158**, 1204-1212.
6. M. I. Alhamid, Y. Daud, A. Surachman, A. Sugiyono, H. Aditya, T. J. R. Mahlia and S. E. Reviews, *Renewable Sustainable Energy Reviews*, 2016, **53**, 733-740.
7. C. Xia, H. Wang, J. K. Kim and J. J. A. F. M. Wang, *Advanced Functional Materials*, 2021, **31**, 2008247.
8. W. Zhou, W. Li, J.-Q. Wang, Y. Qu, Y. Yang, Y. Xie, K. Zhang, L. Wang, H. Fu and D. J. J. o. t. A. C. S. Zhao, *Journal of the American Chemical Society*, 2014, **136**, 9280-9283.
9. D. Ma, D. Sun, Y. Zou, S. Mao, Y. Lv, Y. Wang, J. Li, J.-W. J. J. o. c. Shi and i. science, *Journal of colloid interface science*, 2019, **549**, 179-188.
10. A. Augustin, C. Chuaicham, M. Shanmugam, B. Vellaichamy, S. Rajendran, T. K. Hoang, K. Sasaki and K. J. N. A. Sekar, *Nanoscale Advances*, 2022, **4**, 2561-2582.
11. L. Yu, G. Zhang, C. Liu, H. Lan, H. Liu and J. J. A. C. Qu, *ACS Catalysis*, 2018, **8**, 1090-1096.
12. Y. Zhang, D. Ma, J. Li, C. Zhi, Y. Zhang, L. Liang, S. Mao and J.-W. J. C. C. R. Shi, *Coordination Chemistry Reviews*, 2024, **517**, 215995.
13. M. Shanmugam, C. Chuaicham, A. Augustin, K. Sasaki, P. J. Sagayaraj and K. J. N. J. o. C. Sekar, *New Journal of Chemistry*, 2022, **46**, 15776-15794.
14. M. S. Yesupatham, A. Augustin, N. Agamendran, B. H. Honnappa, M. Shanmugam, P. J. Sagayaraj, T. Ganesan, N. C. S. Selvam, K. J. S. E. Sekar and Fuels, *Sustainable Energy Fuels*, 2023.
15. D. Ma, J. Chen, J. Li, X. Ji and J.-W. J. J. o. M. C. A. Shi, *Journal of Materials Chemistry A*, 2024, **12**, 12293-12324.
16. C. Goodeve and J. J. T. o. t. F. S. Kitchener, *Transactions of the Faraday Society*, 1938, **34**, 570-579.
17. Y. Zou, S. Li, D. Zheng, J. Feng, S. Wang, Y. Hou and G. J. S. C. C. Zhang, *Science China Chemistry*, 2024, 1-9.
18. A. Fujishima and K. J. n. Honda, *nature*, 1972, **238**, 37-38.
19. C. Hu, Y.-H. Lin, M. Yoshida, S. J. A. A. M. Ashimura and Interfaces, *ACS Applied Materials*, 2021, **13**, 24907-24915.
20. D. Ma, Z. Zhang, Y. Zou, J. Chen and J.-W. J. C. C. R. Shi, *Coordination Chemistry Reviews*, 2024, **500**, 215489.
21. B. Debnath, S. Singh, S. M. Hossain, S. Krishnamurthy, V. Polshettiwar and S. J. L. Ogale, *Langmuir*, 2022, **38**, 3139-3148.
22. H. Wang, M. Li, Q. Lu, Y. Cen, Y. Zhang, S. J. A. s. c. Yao and engineering, *ACS sustainable chemistry*, 2018, **7**, 625-631.
23. P. Kumar, E. Vahidzadeh, U. K. Thakur, P. Kar, K. M. Alam, A. Goswami, N. Mahdi, K. Cui, G. M. Bernard and V. K. J. J. o. t. A. C. S. Michaelis, *Journal of the American Chemical Society*, 2019, **141**, 5415-5436.
24. Q. Wang, S. Li, D. Zheng, S. Wang, Y. Hou and G. J. A. A. E. M. Zhang, *ACS Applied Energy Materials*, 2024.
25. Q. Wang, G. Zhang, W. Xing, Z. Pan, D. Zheng, S. Wang, Y. Hou and X. J. A. C. Wang, *Angewandte Chemie*, 2023, **135**, e202307930.
26. B. K. Raja, M. Govindaraj, M. K. Muthukumaran and S. J. N. J. o. C. Ramar, *New Journal of Chemistry*, 2024.
27. D. Gao, Y. Zhang, Z. Zhou, F. Cai, X. Zhao, W. Huang, Y. Li, J. Zhu, P. Liu and F. J. J. o. t. A. C. S. Yang, *Journal of the American Chemical Society*, 2017, **139**, 5652-5655.
28. Y. Wang, Z. Chen, P. Han, Y. Du, Z. Gu, X. Xu and G. J. A. C. Zheng, *ACS Catalysis*, 2018, **8**, 7113-7119.
29. J. Tian, Y. Sang, Z. Zhao, W. Zhou, D. Wang, X. Kang, H. Liu, J. Wang, S. Chen and H. J. s. Cai, *small*, 2013, **9**, 3864-3872.

View Article Online
DOI: 10.1039/D4TA00476K

30. W. Zou, Y. Shao, Y. Pu, Y. Luo, J. Sun, K. Ma, C. Tang, F. Gao and L. J. A. C. B. E. Dong, *Applied Catalysis B: Environmental*, 2017, **218**, 51-59.
31. M. A. Sha, G. Mohanan, L. Elias, T. Bhagya, S. J. M. C. Shibli and Physics, *Materials Chemistry Physics*, 2023, **294**, 127019.
32. M.-y. LIU, J.-y. WANG, D. Lian, L. Xian, L. J. J. o. F. C. ZHANG and Technology, *Journal of Fuel Chemistry*, 2022, **50**, 243-249.
33. B. Wu, T. Sun, N. Liu, L. Lu, R. Zhang, W. Shi, P. J. A. A. M. Cheng and Interfaces, *ACS Applied Materials Interfaces*, 2022, **14**, 26742-26751.
34. J. Song, F. Wu, Y. Lu, X. Zhang and Z. J. A. A. N. M. Li, *ACS Applied Nano Materials*, 2021, **4**, 4800-4809.

The data supporting this article have been included as part of the manuscript and Supplementary Information.

View Article Online
DOI: 10.1039/D4YA00476K